



Cite this: DOI: 10.1039/d3cp01848b

Cross diffusion governs an oscillatory instability in a ternary mixture with the Soret effect

 Berin Seta, ^a Ane Errarte, ^b Aliaksandr Mialdun, ^c Ilya I. Ryzhkov, ^{de} Mounir M. Bou-Ali ^b and Valentina Shevtsova ^{*bf}

In a ternary mixture with the Soret effect, the interplay between cross-diffusion, thermodiffusion, and convection can lead to rich and complex dynamics including spatial patterns and oscillations. We present an experimental and three-dimensional numerical study of dynamic regimes in the toluene–methanol–cyclohexane ternary mixture with the Soret effect in the geometry of a thermogravitational column. An important feature of the system is that for the first component, toluene, the Soret and thermodiffusion coefficients have opposite signs, which triggers the oscillatory instability. Our experiments and numerical analysis show that the primary long-wave instability manifests itself in the form of a standing wave, and the secondary one emerges in the form of a swinging pattern. The computational model provides insight into the role of cross-diffusion coefficient D_{12} in the emergence and development of oscillatory instability. This study demonstrates that the long-wave oscillatory instability in transverse direction occurs only within a limited range of the D_{12} values and outside of this range it decays to a stationary pattern of either Turing-like or monotonic instability.

 Received 22nd April 2023,
 Accepted 17th May 2023

DOI: 10.1039/d3cp01848b

rsc.li/pccp

1 Introduction

In ternary mixtures, there are three species that interact with each other through cross-diffusion. Cross-diffusion refers to the mutual transport of one species caused by the gradient of another species. Thus, each species is transported not only by its own concentration gradient but also by the gradient of the other two species. The Soret effect (also thermodiffusion) describes an establishment of a composition gradient in a multicomponent fluid mixture subjected to a temperature gradient. When thermodiffusion and convective flow are present in a ternary system, the competition between cross-diffusion, thermodiffusion and convection can be enhanced resulting in oscillatory instability.

This cross-coupling effect of heat and mass transfer has been successfully investigated in binary liquid mixtures. Binary coefficients in the associated subsystems may provide a hint about the sign and order of magnitude of Soret coefficients in the ternary system, but not their values.^{1,2} Experiments with

ternary mixtures are still rare as they impose significant difficulties, related to the complexity of extracting the values of coefficients from the measured quantities (*e.g.* optical properties of the media) and the stability requirements for motionless state or specific convective flow in the experimental cell volume.

Denoting the mass fraction of component i by w_i (thus $w_1 + w_2 + w_3 = 1$), we can write the diffusive fluxes of the independent components ($i = 1, 2$) in a ternary mixture as

$$J_1 = -\rho(D_{11}\nabla w_1 + D_{12}\nabla w_2 + D'_{T1}\nabla T) \quad (1)$$

$$J_2 = -\rho(D_{21}\nabla w_1 + D_{22}\nabla w_2 + D'_{T2}\nabla T) \quad (2)$$

where D_{ik} are the Fick diffusion coefficients and D'_{Ti} are the thermodiffusion coefficients. In the stationary state, the diffusion fluxes vanish ($j_i = 0$), and the concentration gradients are proportional to the temperature gradient

$$\nabla w_i = -S'_{Ti}\nabla T, \quad i = 1, 2, \quad (3)$$

where the Soret coefficients (S'_{Ti}) are determined as

$$S'_{Ti} = \sum_{k=1}^2 (D^{-1})_{ik} D'_{Tk}, \quad \sum_{i=1}^3 S'_{Ti} = 0, \quad (4)$$

$(D^{-1})_{ik}$ denotes an element of the inverse diffusion matrix. Thus, six unknown quantities, four diffusion and two thermodiffusion coefficients, have to be determined in the course of experiments. From the Soret experiment in a ternary mixture,

^a Department Civil and Mechanical Engineering, Technical University of Denmark, Denmark

^b Mechanical and Manufacturing Department, (MGEP), Mondragon University, Loramendi 4, Mondragon, 20500, Spain. E-mail: x.shevtsova@mondragon.edu

^c Free University of Brussels (ULB), Brussels, Belgium

^d Institute of Computational Modelling SB RAS, Akademorodok 50-44, 660036 Krasnoyarsk, Russia

^e Siberian Federal University, Svobodnyy 79, 660041 Krasnoyarsk, Russia

^f Ikerbasque, Basque Foundation for Science, Bilbao 20500, Spain

only the Soret coefficients and eigenvalues of the diffusion matrix can be determined; thus, the elements of the diffusion matrix have to be measured separately.^{3,4} The values of the Fick diffusion coefficients depend on the order of the components, since for a ternary mixture the fluxes of two independent components are written out explicitly, while the third component serves as a reference component. In addition, they depend on the reference frame. Here, the mass-fixed reference frame is used, and the mixture components are numbered in descending order of density, *i.e.*, the first component is the denser one.

The density gradients caused by temperature non-uniformity may lead to hydrodynamic instability in mixtures.^{5,6} This may significantly affect the quality of the Soret experiments. The existing laboratory technique may provide reliable measurements in ternary systems with positive Soret coefficients. The opportunity of analyzing several ternary mixtures in convection-free environment, on the ISS,⁷ within the frame of the DCMIX program served as a strong motivation for ground experiments, associated numerical simulations and theory. An important goal of the microgravity experiments was to establish a reliable set of guaranteed convection free reference data for the validation and calibration of present and future ground based measurements. Accordingly, the same systems were studied in ground experiments as in microgravity conditions: *n*-dodecane–isobutylbenzene–tetralin,^{8,9} toluene–methanol–cyclohexane,^{10,11} water–ethanol–triethylene,^{12,13} fullerene–tetralin–toluene,^{14,15} and polystyrene–toluene–cyclohexane.¹⁶

One of the first experiments with truly ternary mixtures were conducted using thermogravitational column.¹⁷ Nowadays, measurements of thermodiffusion coefficients in ternary mixtures are carried out by the two approaches: thermogravitational column^{18,19} and optical methods^{3,20} or their combination.²¹ This work centers on the investigation of the Soret separation in a thermogravitational column (TGC) and its stability. The stability of the Soret driven convection in a ternary mixture placed between infinite vertical walls was examined with respect to long^{22,23} and finite^{24,25} wavelength perturbations. The linear stability analysis in these works showed that stability of the flow primarily depends on the sign of the net separation ratio Ψ ²⁶

$$\Psi = \psi_1 + \psi_2, \quad \psi_i = -(\beta_{w_i}/\beta_T)S'_{Ti}, \quad (5)$$

$$\beta_{w_i} = -\frac{1}{\rho} \frac{\partial \rho}{\partial w_i} \Big|_{T_0, w_{j0}}, \quad \beta_T = -\frac{1}{\rho} \frac{\partial \rho}{\partial T} \Big|_{T_0, w_{j0}}.$$

Here β_{w_i} and β_T are the solutal and thermal expansion coefficients, respectively. If $\Psi > 0$, then the preferred instability is the longitudinal mode, while for $\Psi < 0$, unstable transverse modes prevail. This is true when ψ_i of independent components have the same signs, while either scenario may hold when they take opposite signs.^{24,25}

Till now, the role of cross-diffusion, the phenomenon in which a concentration gradient of one component induces a flux of another component, has generally been not considered in systems with the Soret effect. This is also due to the lack of data on diffusion and especially thermodiffusion coefficients, since the latter can only be measured in a stable system. This issue has

been resolved by measuring thermodiffusion coefficients under microgravity conditions in the several state points of toluene (T)–methanol (M)–cyclohexane (Ch) mixture.^{10,11} The diffusion coefficients for this mixture were measured by Grossmann & Winkelmann^{27,28} and supported by molecular dynamic simulation.²⁹ Based on these data, the first numerical study of this mixture was devoted to revealing the flow patterns in a gravitational field in the geometry of the Soret cell.³⁰ The analysis revealed motionless, metastable, and convective patterns depending on initial temperature of the system.

This work presents experimental, numerical and analytical study of concentration and flow patterns and their stability in toluene (T)–methanol (M)–cyclohexane (Ch) mixture in the geometry of thermogravitational column. The mixture has a demixing zone and large region with negative Soret coefficients,³¹ see the Gibbs triangle in Fig. 1(a). The study focuses on the state point #1 with composition 0.62 (T)–0.31 (M)–0.07 (Ch), called the reference point, which was measured on the ISS. This reference point has several intriguing thermodynamic properties: thermodiffusion (D'_{Ti}) and Soret coefficients (S'_{Ti}) have opposite signs; furthermore, ψ_1 is almost equal to $-\psi_2$ indicating that the net separation ratio is close to zero. The evolution of such a system was considered in the geometry of the Soret cell with different initial temperatures leading to several stationary patterns.³⁰ The pioneer results about the oscillatory instability were shortly presented in the letter.³² Here, we provide a deep insight into the development and existence of oscillatory instability in a ternary mixture placed in a thermogravitational column. We complement our study with experiments in the vicinity of the point where the oscillatory instability was found, determine the region where the oscillatory instability exists and show the existence of other types of instability.

2 Problem formulation

2.1 Liquid system under consideration

We consider a ternary mixture of toluene (T)–methanol (M)–cyclohexane (Ch), Fig. 1(a). The components are numbered according to the density decrease: toluene (component 1), methanol (component 2) and cyclohexane (component 3). The Soret vectors of the system are shown in binary subsystems on the sides of the Gibbs triangle. The concept of the Soret vector in a binary or ternary mixture is as follows:¹ the coordinates of the blue (red) part of the vector corresponding to the concentration change due to temperature decrease (increase). The two half-vectors, symmetrically located around the mean concentration, do visually illustrate the relative strength of the Soret effect and its sign. In the case of a positive (negative) Soret effect, the blue side of the vector is directed towards an increase (decrease) in the mass (molar) fraction of the component. According to Fig. 1(a) the Tol–MeOH mixture exhibits the strongest Soret effect in the region around an equal mass fraction of the components.

The Soret coefficients in the state point #1, the reference point, were measured on the ISS.¹¹ The two state points (#2 and #4) close

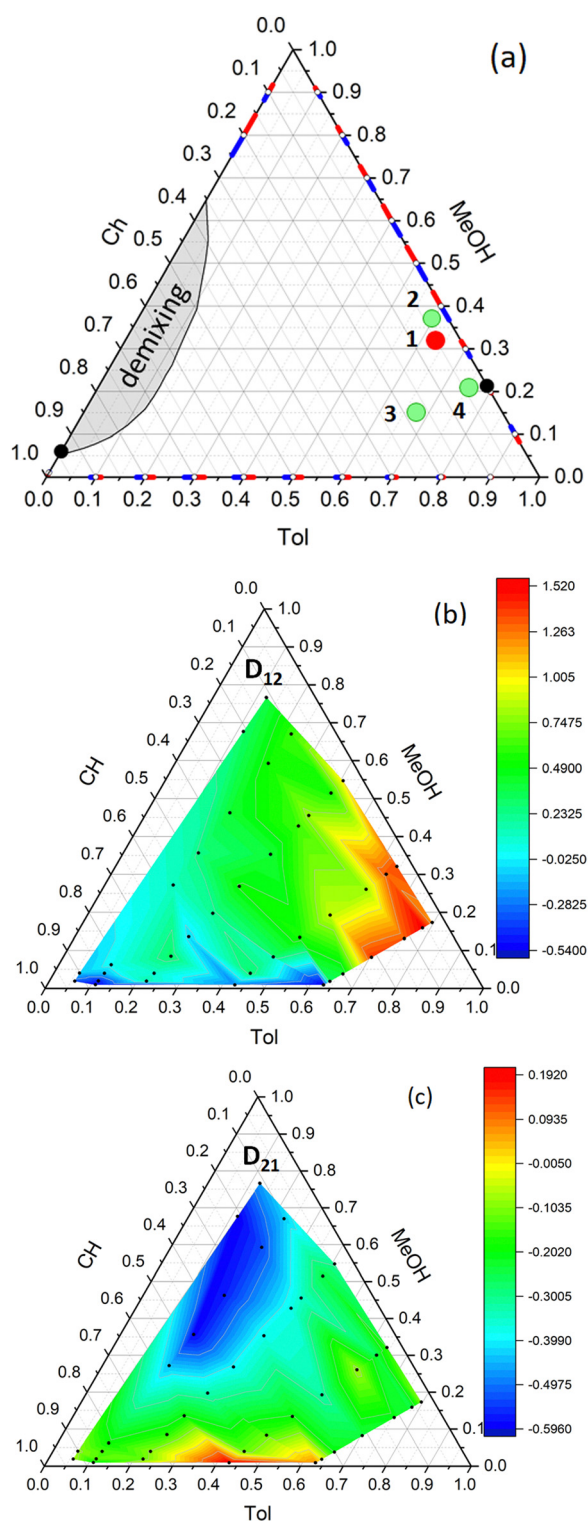


Fig. 1 (a) The Gibbs triangle with the points analyzed in this study and the Soret vectors on the sides.¹ Point 1 is pivotal in this study. The black dots on binary sides (Tol–Ch and MeOH–Ch) indicate the sign change of the Soret coefficient, *i.e.*, $S_{T,\text{bin}} = 0$. Blue side of the Soret vector is aimed at increasing the heavier component content in the corresponding binary mixture Tol–Ch (bottom), Tol–Ch (left side) and MeOH–Ch (right side). (b) and (c) The isolines maps of cross-diffusion coefficients for D_{12} and D_{21} . The units on the sides of the Gibbs triangles are expressed in mass fractions. The units on the color bars are $D_{ij}/10^{-9} \text{ m}^2 \text{ s}^{-1}$.

to the binary boundary are chosen so that one of them should have a large Soret effect and the other almost no effect. The choice of point #4 is associated with a clear difference in the cross-diffusion coefficient D_{12} . The physical properties of the mixtures under consideration are given in Table 1. The data for the point #1 correspond to their values reported by Mialdun *et al.*¹¹ The properties of other state points were measured in the course of this work. The diffusion and thermodiffusion coefficients are listed in Table 2. The original diffusion coefficients^{27,28} were recalculated to the mass-fixed reference frame and taking into account the different order of components.³³ Here we would like to draw the attention to the value of cross-diffusion D_{12} , which is almost three times larger than the main element D_{22} . Maps of the cross-diffusion coefficients on the Gibbs triangle are given in Fig. 1(b) and (c), which illustrate that D_{12} is large in the region under consideration, and its value varies between the selected state points. The other cross-diffusion coefficient, D_{21} , exhibits a nearly uniform distribution being small and negative in this region.

The processing of the ISS experiments reveals that the reference point, #1 in Fig. 1(a), is very close to the stability boundary, since the net separation ratio is close to zero, $\Psi = -6 \times 10^{-4}$, and even depending on the processing methodology it can be slightly positive or negative.¹¹ An intriguing point of the considered mixture is the sign of the D'_{Ti} in Table 2, which was calculated from the measured diffusion and Soret coefficients. The sign of thermodiffusion coefficient D'_{Ti} is negative, while the sign of S'_{Ti} is positive. The relationship between D'_{Ti} and S'_{Ti} is the following

$$D'_{T1} = S'_{T1}D_{11} + S'_{T2}D_{12}, \quad (6)$$

$$D'_{T2} = S'_{T1}D_{21} + S'_{T2}D_{22}. \quad (7)$$

The main diffusion coefficients D_{ii} are positive,³³ and the sign change between S'_{T1} and D'_{T1} is due to the second term on right-hand side in eqn (6). Here, the value of cross-diffusion D_{12} approaches D_{11} , while $|S'_{T2}| > 2|S'_{T1}|$ and they have opposite signs. Thus, there are two reasons for the sign change: the large cross-diffusion and the opposite signs of the first and second terms. To the best of our knowledge, there is no other mixture when S'_{T1} and D'_{T1} have different signs. In a binary system, the signs of the Soret and thermodiffusion coefficients coincide.

2.2 Experimental

Most measurements of thermodiffusion and Soret coefficients in ternary mixtures are carried out by optical detection of the change in refractive index using two light sources. In laboratory experiments, a thermogravitational microcolumn with a contactless optical detection system operating on the principle of Mach–Zehnder interferometer was used. The sketch of the set-up is shown in Fig. 2. The liquid is placed in narrow slot between two plates with different temperatures. The imposed horizontal temperature gradient induces horizontal gradients of composition due to the Soret effect. It also results in convective flow driven by buoyancy force. The horizontal separation of

Table 1 Physical properties of the toluene (1)–methanol (2)–cyclohexane (3) mixture with composition in mass fractions w_i [kg kg⁻¹] at $T_0 = 298.15$ K: density ρ , thermal $\beta_T = -\rho_0^{-1}\partial\rho/\partial T$ and solutal $\beta_C = -\rho_0^{-1}\partial\rho/\partial C$ expansion coefficients, dynamic μ and kinematic ν viscosity, thermal conductivity k and diffusivity χ , the Prandtl number $Pr = \nu/\chi$. All data are measured in this work

Point	w_1	w_2	w_3	ρ (kg m ⁻³)	$\beta_T/10^{-3}$ (K ⁻¹)	β_{w1}	β_{w2}	$\mu/10^{-3}$ (Pa s)	$\nu/10^{-6}$ (m ² s ⁻¹)	$k/10^{-1}$ (W m ⁻¹ K ⁻¹)	$\chi/10^{-8}$ (m ² s ⁻¹)	Pr
#1	0.62	0.31	0.07	830.03	1.158	-0.140	-0.048	0.560	0.675	1.466	7.52	8.91
#2	0.60	0.35	0.05	829.55	1.159	-0.137	-0.047	0.562	0.678	1.495	7.59	
#3	0.65	0.15	0.2	828.26	1.16	-0.128	-0.029	0.545	0.658	1.343	7.29	
#4	0.75	0.22	0.03	841.56	1.131	-0.137	-0.043	0.553	0.657	1.427	7.45	

Table 2 The mass diffusion coefficients $D_{ij}/10^{-9}$ m² s⁻¹, the Soret coefficients $S_{Ti}/10^{-3}$ K⁻¹, the thermodiffusion coefficients $D'_{Ti}/10^{-13}$ m² s⁻¹ K⁻¹, separation ratios ψ_i , and the net separation ratio Ψ of the toluene (0.62)–methanol (0.31)–cyclohexane (0.07) mixture (in mass fractions)

D_{11}	D_{12}	D_{21}	D_{22}	S'_{T1}	S'_{T2}	D'_{T1}	D'_{T2}	ψ_1	ψ_2	Ψ
2.244	1.337	-0.226	0.551	0.387	-1.145	-6.6244	-7.1836	0.0467	-0.0473	-0.0006

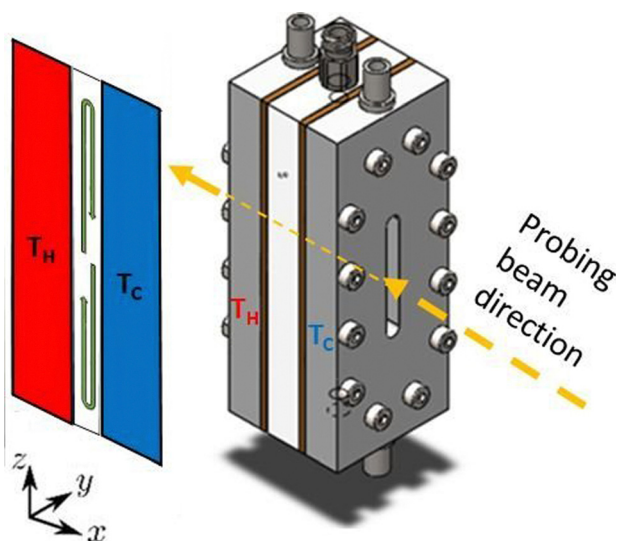


Fig. 2 Drawing of the TG-microcolumn (on the right) and its sketch in the direction of temperature gradient (left).

components in combination with the vertical convective current leads to an enhanced separation between the top and bottom ends.

The refractive index of the mixture $n(T, C)$ changes with temperature and concentration variation. The refractive index variation (Δn) between two points at different heights is measured with an interferometer using two lasers with different wavelength $\lambda_1 = 633$ nm and $\lambda_2 = 473$ nm. The interferogram processing obtained with the Mach-Zehnder interferometer gives the change in the optical phase $\Delta\phi$ between two points.³⁴ Then, the change in the refractive index is determined from the optical phase variation

$$\Delta n_i = n(x, z) - n_0 = \frac{\lambda_i}{2\pi L_x} \Delta\phi \quad (8)$$

where λ_i is the wavelength and L_x is the thickness of the liquid in the direction of the optical pathway. These variations in the measured refractive indices allow the variation in concentrations to be determined through solving a system of linear

equations:

$$\begin{pmatrix} \Delta n_1 \\ \Delta n_2 \end{pmatrix} = \begin{pmatrix} \frac{\partial n_1}{\partial w_1} & \frac{\partial n_1}{\partial w_2} \\ \frac{\partial n_2}{\partial w_1} & \frac{\partial n_2}{\partial w_2} \end{pmatrix} \begin{pmatrix} \Delta w_1 \\ \Delta w_2 \end{pmatrix} \quad (9)$$

The optical contrast factors ($\partial n_i/\partial w_j$) should be measured in advance.^{35,36} The contrast factor matrix inversion can be problematic as it is often ill-conditioned.^{20,36,37} This can lead to amplification of the error after the conversion from the refractive index to the concentration space. The thermodiffusion coefficient, D'_{Ti} , is determined from the known variations of compositions in mass fraction:

$$D'_{Ti} = \frac{L_x^4 g \rho \beta_T \Delta w_i}{504 \mu \Delta z} \quad (10)$$

here Δz is the distance between points, at which optical phase is measured; other quantities are defined in Table 1. The detail description of the column and processing of the results could be found in previous works.^{21,38} For reliable measurements of thermodiffusion coefficients, the total density gradient, which results from the concentration gradients of independent mixture components, must be gravitationally stable.²⁴ In addition, the convective flow in the vertical direction of the column must be stationary and stable. This flow should turn around only near the top and bottom walls, so it can be characterized as one-vortex flow.

2.3 Governing equations

Computer simulations were first run for state points #1 and #2 and then extended to the region of compositions beyond the experimental points using assumptions based on the Soret vector.¹ Mathematical model considers that walls are impermeable, the fluid is incompressible and the flow is Newtonian. The geometry closely corresponds to the laboratory setup, see Fig. 3. The horizontal temperature gradient induces horizontal gradients of composition due to the Soret effect and also results in convective flow driven by buoyancy force. We solve numerically three-dimensional time-dependent Navier–Stokes and mass

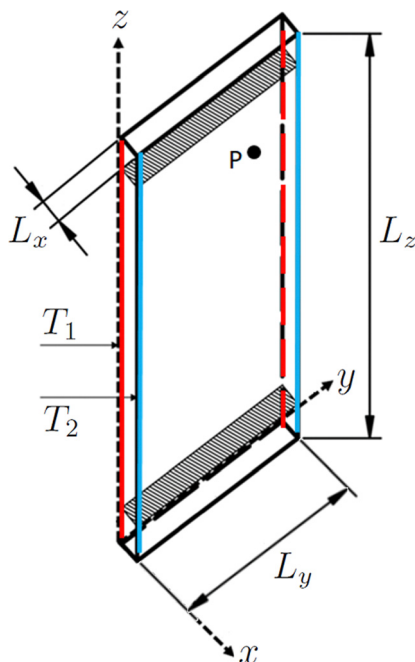


Fig. 3 The TGC geometry and coordinate system used in numerical simulations. The inner cavity has a height of $L_z = 30$ mm, a gap width of $L_x = 0.51$ mm, and a depth of $L_y = 3$ mm. Point "P" has coordinates $\{x = 0.255$ mm, $y = 2.5$ mm, $z = 24$ mm}.

transfer equations in Boussinesq approximation.^{26,39}

$$\frac{\partial \vec{V}}{\partial t} + \vec{V} \cdot \nabla \vec{V} = -\frac{1}{\rho_0} \nabla p + \nu \Delta \vec{V} + \vec{g} \rho^* \quad (11)$$

$$\text{div} \vec{V} = 0, \quad (12)$$

$$\frac{\partial T}{\partial t} + \vec{V} \cdot \nabla T = \chi \Delta T, \quad (13)$$

$$\frac{\partial w_1}{\partial t} + \vec{V} \cdot \nabla w_1 = D_{11} \Delta w_1 + D_{12} \Delta w_2 + D'_{T1} \Delta T, \quad (14)$$

$$\frac{\partial w_2}{\partial t} + \vec{V} \cdot \nabla w_2 = D_{21} \Delta w_1 + D_{22} \Delta w_2 + D'_{T2} \Delta T. \quad (15)$$

Here \vec{V} is the velocity; T is the temperature; p is the difference between total and hydrodynamic pressure; ν is the kinematic viscosity, χ is the thermal diffusivity, D_{ij} are the diffusion coefficients, and D'_{Ti} are the thermodiffusion coefficients.

We assume that the density is a linear function of temperature and composition:

$$\rho^* = \rho_0 [1 - \beta_T (T - T_0) - \beta_{w1} (w_1 - w_{10}) - \beta_{w2} (w_2 - w_{20})].$$

The problem should be completed with the boundary and initial conditions. On the column walls, we impose the no-slip boundary condition and the absence of diffusive fluxes ($J_1 = J_2 = 0$):

$$\vec{V} = 0, \quad (16)$$

$$(D_{11} \nabla w_1 + D_{12} \nabla w_2 + D'_{T1} \nabla T) \cdot \vec{n} = 0, \quad (17)$$

$$(D_{21} \nabla w_1 + D_{22} \nabla w_2 + D'_{T2} \nabla T) \cdot \vec{n} = 0. \quad (18)$$

The lateral vertical walls are kept at different constant temperatures ($T^0 = 298$ K)

$$x = 0: T = T_0 - \Delta T/2, \quad x = L_x: T = T_0 + \Delta T/2, \quad (19)$$

where ΔT is the applied temperature difference. The other four walls are assumed adiabatic

$$\nabla T \cdot \vec{n} = 0. \quad (20)$$

The initial conditions at $t = 0$ are as follows

$$\vec{V} = 0, \quad T = T_0, \quad w_1 = w_{10}, \quad w_2 = w_{20}. \quad (21)$$

2.4 Numerical approach

The open-source solver OpenFOAM was used for solving governing eqn (11)–(15). The problem was solved using dimensional variables (x, y, z). The convective terms used a second order discretization and the time integration was carried out using a second order implicit Crank–Nicholson scheme with an off-centering coefficient equal to 0.9 to stabilise. The momentum and continuity equations were solved using the PIMPLE algorithm and the temperature and concentration equations were solved for each PIMPLE outer iteration securing the convergence. Neumann boundary conditions were implemented with the help of the GroovyBC package. Numerical solutions used in all cases the bi-conjugate gradient method preconditioned by incomplete Cholesky factorization or by the Diagonal-based Incomplete LU method.

3 Results. Experimental observations

3.1 Reference point

Let us recall the uniqueness of state point #1. The Soret S'_{T1} and thermodiffusion D'_{T1} coefficients of toluene have opposite signs and D_{12} is large. The separation ratios ψ_i of independent components are almost equal and have opposite signs leading to a value of the net separation ratio $\Psi = -0.0006$ close to zero.

The laboratory experiments revealed an oscillatory regime, which is demonstrated in Fig. 4 in terms of optical phase for the two selected experiments repeated with a large difference in time. It is important to note that our experiments in TGC for the first time have shown evidence of an oscillatory regime in the Soret experiments in ternary mixture. Previous experimental studies displaying the oscillatory instability dealt with binary mixtures in the geometry of the Soret cell.⁴⁰ So far, the available theoretical predictions in TGC^{22,24} have not been confirmed either by experiments or by 3D non-linear modelling. Our experiments present the first confirmation of the theoretical prediction that an oscillatory instability occurs in mixture where ψ_1 and ψ_2 have different signs. The oscillation period Π recorded in the experiments is about 4000 s.

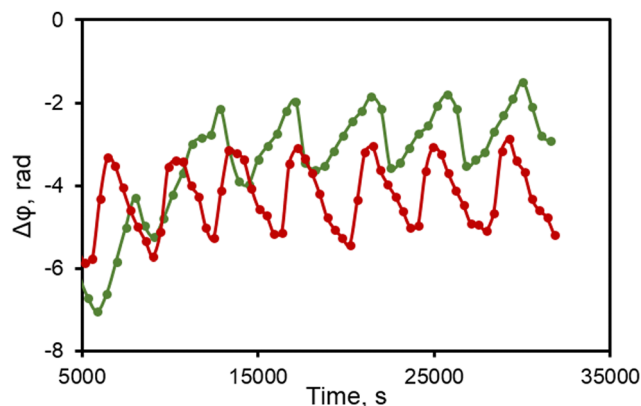


Fig. 4 The optical phase evolution illustrating the oscillatory regime at point #1. The curves correspond to experiments carried out with a time difference of several months using laser with $\lambda = 473$ nm and $\Delta T = 8$ K.

3.2 Neighboring points

To explore further the instability and the region of its existence, experiments were carried out in the neighboring state points. The experiments in the two nearest points #2 and #4 lead to different but in some way expected result. Fig. 5 illustrates that the time evolution of the optical phase at these points, $\Delta\phi$, is completely different. The random oscillations around zero at point #4 could be associated with noise, suggesting the absence of the Soret effect. Indeed, one can see in Fig. 1(a) that point #4 is very close to the region where binary subsystem exhibits a sign change (marked with the black dot) and the Soret coefficient passes through zero. In addition, a decrease in the length of the Soret vector asserts a decrease of the Soret separation. From these observations we can conclude that the Soret separation at the state point #4 is negligible.

In contrast, the Soret separation at point #2 (the blue symbols) is quite strong and stable. This is also expected since the state point is closer to the binary subsystem with a strongly positive Soret separation and, in addition, pioneering experiment in the geometry of the Soret cell³¹ predicted hydrodynamic stability in this region. On the quantitative side, $\Delta\phi \sim 9$ rad, and this allows to determine the thermodiffusion coefficients D'_{Ti} .

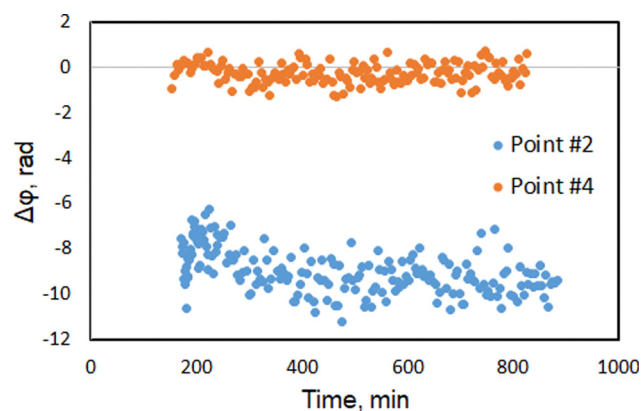


Fig. 5 The evolution of optical phase $\Delta\phi$ at points #2 (blue symbols) and #4 (red symbols) at $\lambda = 473$ nm. Experiments were conducted at $\Delta T = 8$ K.

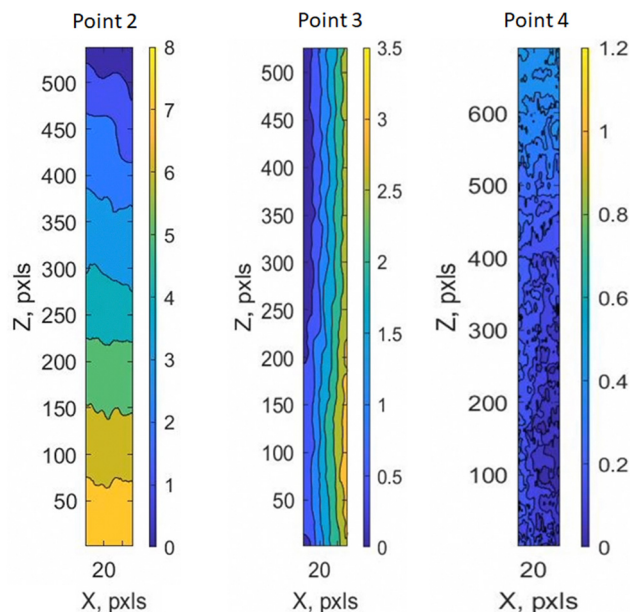


Fig. 6 Typical concentration patterns observed at the experiments at points #2, #3 and #4 at $\lambda = 473$ nm and $\Delta T = 8$ K shown via isolines of $\Delta\phi$. The units on the color bars are $\Delta\phi$ in radians.

Further insight into the system behavior can be gained from the concentration patterns in Fig. 6 shown through the optical phase. We do not specify the time moments for these patterns, since they are typical over the entire duration of the Soret experiment. At point #2, the linear phase distribution in height indicates a steady convective flow in the TGC and corresponds to a stable density profile and, consequently, to the steady concentration profile. The knowledge of vertical concentration gradients allows one can determine the thermodiffusion coefficients, see eqn (10).

The pattern at point #3 also illustrates stationary convective flow. However, the $\Delta\phi$ profile develops in a horizontal rather than a vertical direction. Consistently, there is no stable density profile in the vertical direction and the system maintains such a pattern, presumably due to convection in the transversal direction. From these results we may suggest that this is a kind of monotonic instability. At point #4, the pattern reveals some random motion of a very low intensity in accordance with the $\Delta\phi$ evolution in Fig. 5.

The above analysis has shown that state point #2 is the only point, for which the thermodiffusion coefficient can be retrieved. An obstacle to the accurate determination of D'_{Ti} is the poor conditioning of the matrix of optical contrast factors,³⁶ see eqn (9). We have conducted the Soret experiment at state point #2 using two different instruments: microcolumn, see Section 2.2, and the conventional TGC of the height $L_z = 500$ mm with the inner cross-section $1 \text{ mm} \times 50 \text{ mm}$.¹⁸ The optical approach used in microcolumn exhibits a problem due to a relatively large condition number,³⁶ which is about $\mathcal{K} \sim 80$. A high condition number indicates that a small change in the input (Δn_i) can lead to a large change in the output (Δw_i). Thus, it can increase the uncertainty in the measurement,

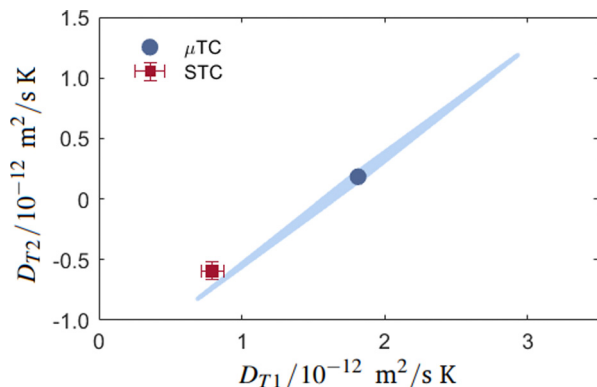


Fig. 7 Thermodiffusion coefficients measured at point #2 using the two TGCs: micro-column with Mach–Zehnder interferometer (μ TGC) and the short TGC (TGC) of a height 500 mm. The blue shade shows the distribution area of the coefficients measured in μ TGC which have a large elongated error bar due to the large condition number. $\lambda_1 = 473$ nm and $\lambda_2 = 633$ nm, $\Delta T = 8$ K.

resulting in a large error bar and can complicate the determination of the true measurement value. The thermodiffusion coefficients obtained in the different TGC instruments are:

$$(\mu\text{TGC}) \quad D'_{T1} = 1.81 \times 10^{-12} \quad \text{and}$$

$$D'_{T2} = 1.84 \times 10^{-13} \text{ m}^2 \text{ s}^{-1} \text{ K}^{-1},$$

$$(\text{STGC}) \quad D'_{T1} = 7.93 \times 10^{-13} \quad \text{and}$$

$$D'_{T2} = -5.95 \times 10^{-13} \text{ m}^2 \text{ s}^{-1} \text{ K}^{-1}.$$

From the first look, the results shown in Fig. 7 reveal the considerable difference between measurements. Here one should be aware of the asymmetric nature of error propagation in the Soret experiment.^{11,37} The error bar forms a very elongated ellipsoid instead of an isotropic cloud around solution point $[D'_{T1}, D'_{T2}]$, and practically degenerates into a line. This elongated ellipsoid is illustrated in Fig. 7 by the blue shading. The second solution (shown by the square) obtained in the conventional TGC experiment, lies within the error bar of the experiment with optical probing. This solution has a lower error bar because the associated condition number composed by the refractive index and density variations, is smaller. We will not further discuss the uncertainty of the results obtained, since our main goal is to understand the nature of oscillatory instability. Since the two solutions reveal different signs of D'_{T2} , the validity of each of them can be verified in the future non-linear simulations aimed at studying the limitations of the scattering region. The output, which will be utilized here, is that the experiments at the considered four state points evidence different types of convective behavior.

4 Numerical results

Numerical simulation was carried out using the mixture physical properties at the reference point #1, and in the case

of a parametric study, only the cross-diffusion coefficient D_{12} was varied.

4.1 Instability in the reference point

Time-dependent non-linear simulations revealed oscillatory behavior of the mixture. The instability leads to the development of a time-periodic three-dimensional flow F , which can be represented at leading order as

$$F \approx F_{\text{st}} + F^*,$$

where F_{st} is the undisturbed stationary flow and F^* is its oscillatory part. Here, F can be any representative quantity, (\vec{V}_p, T, w_i) . The stationary part, F_{st} , called the basic state in linear stability analysis, has an analytical solution for an infinite two-dimensional vertical slot mimicking TGC.²⁶ The solution can be written in the form ($l = L_x/2$)

$$V_x = V_y = 0, \quad V_{z,\text{st}} = V(x), \quad T_{\text{st}} = T(x), \quad (22)$$

$$w_{i,\text{st}} = w_i(x, z), \quad \frac{\partial w_{i,\text{st}}}{\partial z} = -\frac{504\nu D'_{Ti}}{g\beta_T L_x^4}. \quad (23)$$

In the experiments, the last term in eqn (23) is used for the determination of D'_{Ti} from the measured concentration gradients $\partial w_{i,\text{st}}/\partial z$.

At the reference point, the basic state solution for w_i is unstable, since both thermodiffusion coefficients D'_{Ti} are negative. It means that $\partial w_{i,\text{st}}/\partial z > 0$ for toluene and methanol, which are the heaviest components of the mixture. This also means that an unstable density stratification develops over time.

To trace further the oscillatory behaviour of the mixture, the numerical results will be presented at the point P shown in Fig. 3. This point is quite high and sensitive to the accumulation of heavier components and the onset of instability. But still it is below the area where the convective flow at the top begins to turn around. The time evolution of the oscillatory parts of the concentrations fields w_i^* are shown in Fig. 8(a) at this point, and it makes clear that the waveforms for toluene and methanol are very different. At a very early stage ($t < 600$ s), the black curve is slightly negative, which means that the toluene drifts downwards, as the Soret coefficient S'_{T1} is positive. Since the large cross-diffusion coefficient changes D'_{T1} in a non-trivial way, contrary to the Soret sign, toluene begins to be transported upward and attains the steady state, which persists up to $t \approx 1700$ s. Then the instability sets in. It takes some time for the system to reach sustained periodic behaviour. On average, the mass flux of methanol is much greater than that of toluene, suggesting its dominant role.

In a TGC, the mass fluxes can be considered separately in horizontal and vertical directions.⁴¹ The mass flux in the vertical direction is formed by the joint action of Soret separation, diffusion and convection. The bottom panel in Fig. 8 illustrates the vertical mass fluxes J_1 and J_2 , which were initially close to zero, but over time the heavier components accumulated at the top and methanol (red curve) became the first to lose stability. The vertical fluxes J_i develop in different manner and over the time the toluene

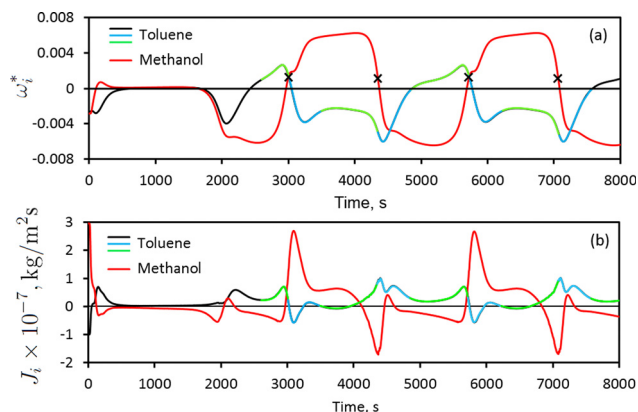


Fig. 8 The oscillation amplitude around a basic state for (a) components and (b) the vertical net mass fluxes of toluene (w_1 , black, green and blue) and methanol (w_2 , red) at the point P . The primary instability appears as a standing wave. The blue color on curves for w_1 , J_1 highlights the regions with the occurrence of swinging instability. The green color on the curves illustrates the diffusion phase of a standing wave. The crosses indicate the time moments when the swinging instability is triggered, the distance between them is a half-period.

flux becomes opposite to the methanol flux, and this triggers oscillatory instability.

We hypothesize that a large cross-diffusion is responsible for the occurrence of oscillations. Just for explanation, let us assume for the moment that cross-diffusion is absent. Then, the thermodiffusion coefficients of both components will have the same signs and both mass fluxes will be co-directed. However, once the cross diffusion is introduced into the system, the Soret coefficient of toluene becomes positive, even though both thermodiffusion coefficients are negative. This means that the concentration gradient of one component can affect the mass flux of the other component, leading to the establishment of mass fluxes with opposite signs. This may lead to the occurrence of oscillatory behavior in the system, depending on the other parameters and conditions. This peculiar behaviour could only happen for high values of D_{12} , which is the case in this mixture.

Cross-diffusion plays an important role in determining the oscillation period. In the studied D_{12} range, two different slopes of the oscillation period $\Pi(D_{12})$ are clearly distinguished, as shown in Fig. 9 by two solid black curves. Starting from their intersection at D_{12}^* (indicated by the yellow line) and moving towards a smaller cross-diffusion ($D_{12} < D_{12}^*$), the oscillation period increases rapidly with a linear and steep slope. When moving towards larger cross-diffusion ($D_{12} > D_{12}^*$), the oscillation period decreases with a much smaller and smoother slope. At this particular value of $D_{12}^* = 1.4 \times 10^{-9} \text{ m}^2 \text{ s}^{-1}$, the net separation ratio Ψ is equal to zero, although the individual ψ_i are non zero. Thus, a branch with a large growth rate corresponds to a negative Ψ , and a branch with a small growth rate corresponds to a positive Ψ . Note, that the examined range of D_{12} corresponds to the small values of the net separation ratio, $-0.015 < \Psi < 0.05$.

The oscillation period at the reference point determined in simulations is $\Pi \approx 2740$ s. This Π value is lower than the

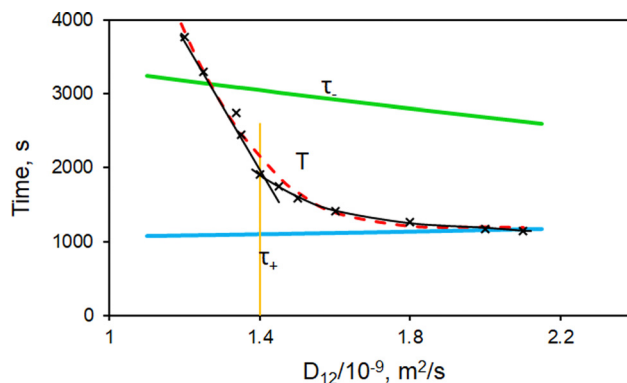


Fig. 9 Connection between oscillation period Π (the red curve) and the characteristic diffusion times τ_{\pm} as D_{12} changes. The black solid curves clearly highlight two different slope on the dependence $\Pi(D_{12})$. The crosses indicate points at which calculations have been conducted. The yellow line illustrates the crossing point, D_{12}^* where the net separation ratio $\Psi = 0$. The red dashed curve is guideline that connects all the data for oscillation period.

experimental one, which is about 4000 s. The discrepancy can be explained by the strong dependence of the oscillation period on the cross-diffusion coefficients, as seen in Fig. 9. This can be partly explained by the argument that the cross-diffusion coefficients are measured with a large uncertainty, which can easily reach 10–20%.^{27,28,42,43} Nowadays, the Taylor dispersion technique is commonly used to measure the diffusion coefficients in a ternary mixture, and it includes four fitting parameters to retrieve coefficients. For the main diffusion coefficients, there is an initial guess from quasi-binary approach. Thus, the uncertainties in the fitted values of main diffusion coefficients are smaller in comparison with those related to the cross-diffusion coefficients. Furthermore, fitting for cross-diffusion can be problematic, because they can change sign or be close to zero, and the initial guess may be far away from the real value and trust region.

4.2 Transverse or longitudinal mode of instability

As already mentioned in the introduction, the linear stability analysis (LSA) in an infinite vertical slot mimicking a TGC indicated^{22,24} that in the case when the separations ratios have opposite signs, an instability can emerge in the form either transversal or longitudinal modes. Furthermore, Zebib²² suggested that transversal mode can be more dangerous, leaving in doubt whether it is monotonic or oscillatory. In the LSA, the instability in longitudinal and transversal directions are considered separately. In the experiments or in non-linear simulations the modes of an oscillatory state cannot be separated as in LSA and involve complex interactions between different modes and non-linear effects.

In order to understand the instability mode, let us analyze the characteristic times of the system. There are several times: the viscous $\tau_{\text{vis}} = L^2/\nu$, the thermal $\tau_{\text{th}} = L^2/\chi$ and two diffusion times $\tau_{\text{dif}} = L^2/\hat{D}_{\pm}$ (τ_+ and τ_-), where

$$\hat{D}_{\pm} = \frac{1}{2} \left(D_{11} + D_{22} \pm \sqrt{(D_{11} - D_{22})^2 + 4D_{12}D_{21}} \right) \quad (24)$$

are the eigenvalues of the diffusion matrix. The characteristic length L can be considered in (x, y, z) directions. Viscous time in all directions and thermal times in (x, y) directions are much smaller than the oscillation period. The diffusion times in the x direction are about 30 s and 90 s and do not match with the characteristic time of oscillations. For y direction, the times are $\tau_- = 2990$ s and $\tau_+ = 1100$ s, which are consistent with the oscillation period and its fastest phases. Based on the analysis of characteristic times, it can be concluded that the instability primarily develops in the yz -direction with a transversal mode.

Fig. 9 also presents the dependence of the diffusion times on D_{12} illustrating correlation of the oscillation period with the diffusion times. It shows that τ_- and τ_+ get closer as D_{12} increases.

4.3 Primary and secondary instabilities

In order to investigate the patterns formation associated with the oscillatory instability, the deviations of the fields from the steady state are analysed. We consider the development of perturbations in yz -plane, where they are most crucial. Usually different types of instability exist in separate domains of parameters. For considered particular mixture with strong cross-diffusion D_{12} leading to opposite signs of S'_{T1} and D'_{T1} , the different types of instabilities are present at the same space of parameters, but they are differently excited. We found out that primary instability emerges as a standing wave and the secondary one occurs at some moments of time in the form of a swing. The feature of a standing wave is the change of rich/poor areas of analysed quantity every half of a period.

We will start the discussion of system nonlinear dynamics with the behaviour of w_2^* , since it has the largest oscillation amplitude and exhibits an instability in the form of a clear standing wave. The snapshots of the concentration field over half-period of oscillations (+ one snapshot for the reference) are given in Fig. 10 (central panel). At the first snapshot, a methanol poor (rich) region is on the left (right) side of the pattern. The subsequent six snapshots illustrate a fast exchange of poor and rich regions of w_2^* . This suggests that in the y direction, the behaviour of methanol has a strong tendency to instability in the form of a standing wave. After the formation of a region with a low w_2^* mass fraction on the right that takes about ~ 500 s, the alignment of isolines and their intensity develop slowly in time; we call this time interval as the diffusion phase. During the exchange between poor/rich regions of methanol, the w_2^* concentration field becomes uniform displaying very small deviation from the basic state, see the second snapshot. Such points in time are marked by crosses in Fig. 8.

Turning next to instability in toluene, w_1^* , we draw the attention to the time moments, when the w_2^* concentration is nearly uniform, *i.e.*, 2nd and 16th snapshots, which also delimits a half of a period. At these moments, the horizontal and vertical mass fluxes of methanol tend to zero; toluene takes the lead and begins swinging (pendulum) motion, which is quite fast, $\tau_{sw} \sim 500$ s, see the large arrow in Fig. 10 (upper panel). Overall picture shows that the swinging also leads to an

exchange of poor/rich regions of toluene and, in the origin, the instability has a form of a standing wave. Interestingly, the w_1^* swinging and the exchange between rich/poor regions of w_2^* occurs simultaneously, but in opposite phase. This active phase is characterized by a strong bursts in the mass fluxes, see the blue part of curves in Fig. 8. At the end of active phase, the components are concentrated on opposite sides of yz -plane. Next, the pattern evolution slows down, and during the following so-called diffusion phase, the vertical alignment of the concentration isolines occurs. It is worth noting that the effect of swinging on the concentration pattern is rather strong, and the w_1^* level lines during the diffusion phase remain slightly inclined, while the w_2^* isolines are straight. During the diffusion phase, the vertical mass fluxes J_1 and J_2 are small and oppositely directed and, J_1 is even close to zero, see Fig. 8, where the diffusion phase is shown in green on curve for w_1^* . Another observation is that the scenario of instability development in the first and the second half-periods is somewhat different, since the swinging begins from different distributions of the concentration fields. The swinging occurs two times per period and, thus, we conclude that its duration, τ_{sw} , is associated with a shorter diffusion time scale, $\tau_+ \approx 2\tau_{sw}$.

Fig. 10 also shows the isolines of stream function in yz -plane (x slightly shifted from $L_x/2$), which, mostly, represents one elongated vortex. The strongest convective flow is observed at the time of swinging. In the diffusion phase, the intensity of convection slows down until the vortex begins to divide into four weak vortices. At this moment, the strength of flow in the transverse direction is the smallest while the oscillation amplitude $|w_1^*|$ approaches its maximum value and serves as the precursor of the upcoming swinging. Further, one elongated vortex is formed again, but with the opposite direction of circulation.

4.4 Impact of D_{12} on oscillatory pattern

We hypothesize that the mismatch in signs between S'_{T1} and D'_{T1} due to large D_{12} is responsible for a pendulum motion of w_1 pattern, and, in addition, this is the motor of the entire oscillatory instability.

To demonstrate this, we performed a series of calculations over a wide range of the D_{12} keeping all other values unchanged, as in Tables 1 and 2. Fig. 9 illustrates that the decrease in D_{12} leads to a longer oscillation period, which is accompanied by a stronger discrepancy in the diffusion times. As D_{12} decreases by $\sim 10\%$ from the reference point, the oscillation period increases by $\sim 35\%$, from $\Pi(\text{ref}) = 2740$ s up to $\Pi = 3770$ s when $D_{12} = 1.2 \times 10^{-9} \text{ m}^2 \text{ s}^{-1}$. To illustrate reorganisation of the oscillatory patterns with change in cross-diffusion, Fig. 11 presents w_1 and w_2 oscillating around the initial state for the reference point (panel b), as well as for smaller (a) and larger values (c) of D_{12} . The graph for the reference point (panel b) differs from Fig. 8(a) by the fact that fluctuations are shown here around the initial state, and in the latter case around the basic state. The comparison between panels presents an evidence that the diffusion phase during the

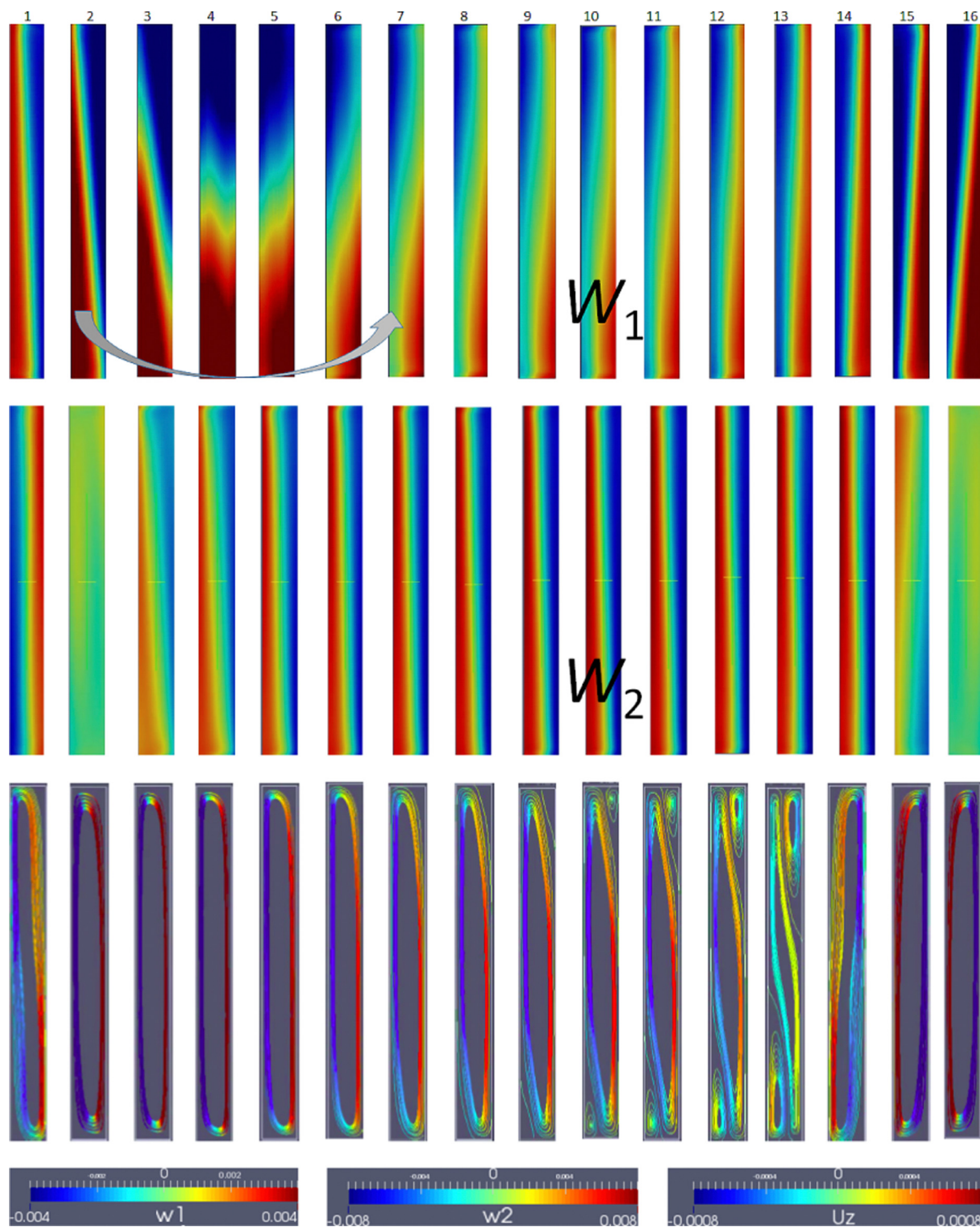


Fig. 10 The evolution of perturbation patterns showing the deviation from the basic state solution for toluene (top), methanol (center) and flow streamlines (bottom) over the half of a period. The concentrations fields for w_1 and w_2 evidence development of a standing wave as a primary instability, which is confirmed by the exchange of rich/poor areas of component mass fraction every half of a period. The large arrow in upper panel illustrates the swinging instability on the basis of standing wave. The snapshots 1–16 correspond to the time moments t (s) = 4200, 4350, 4450, 4550, 4650, 4750, 4850, 4950, 5050, 5150, 5250, 5350, 5450, 5550, 5650, 5720.

oscillation period (the green parts of the curves) decreases significantly with increasing D_{12} .

For example, the duration of the diffusion phase decreases from 1370 s to 240 s when D_{12} changes from $1.2 \times 10^{-9} \text{ m}^2 \text{ s}^{-1}$

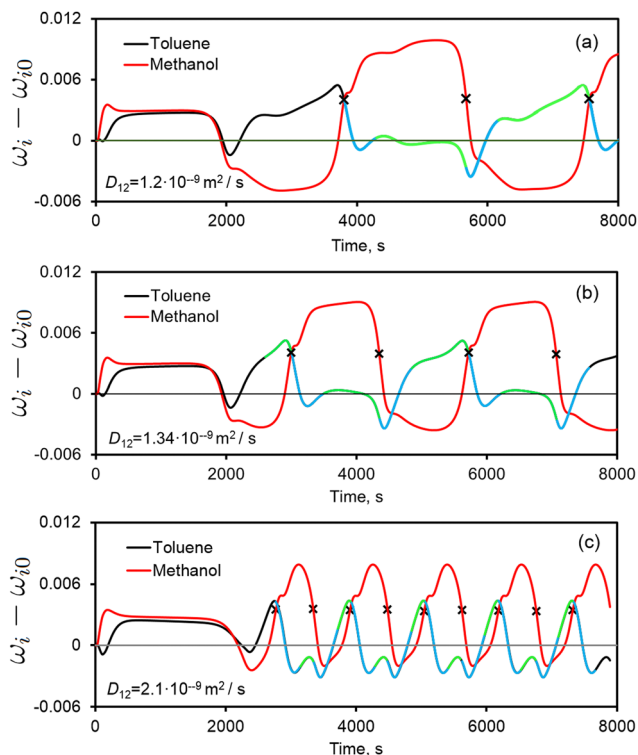


Fig. 11 Reorganization of the oscillatory instability with enhancement of cross-diffusion D_{12} (from top to bottom). The green and blue colors on the toluene (w_1) curves outline swinging and diffusion phases of SW, and for simplicity, methanol (w_2) is shown by uniform red. The oscillations are shown around an initial state at the point P at different D_{12} (a) $D_{12} = 1.2 \times 10^{-9} \text{ m}^2 \text{ s}^{-1}$, (b) $D_{12} = 1.34 \times 10^{-9} \text{ m}^2 \text{ s}^{-1}$ and (c) $D_{12} = 2.1 \times 10^{-9} \text{ m}^2 \text{ s}^{-1}$.

to $2.1 \times 10^{-9} \text{ m}^2 \text{ s}^{-1}$. The drops in the duration of diffusion phase occur much faster at $D_{12} < D_{12}^*$, in accordance with Fig. 9. The swinging time (blue intervals) remains almost unchanged. Thus, an increase in D_{12} reduces the oscillation period due to shrinking of the diffusion phase while preserving the oscillatory swinging motion.

One of the distinct signatures of a standing wave is a node in the middle of pattern that always has zero amplitude. This feature can be observed on the space-time maps in Fig. 12. Indeed, all the maps presenting the oscillation amplitudes ($w_i - w_{i0}$) around the initial state at three distinct values of D_{12} (the same as in Fig. 11) exhibit such a node at mid-depth, $y \sim L_y/2$. Around the node, there is an exchange of rich and poor regions of mixture components. Another distinct sign of a standing wave is that a wave oscillates in time, but its peak amplitude profile does not move in space, this is clearly seen in all the panels.

The topology of all the space-time maps in the y direction in Fig. 12 confirms the presence of a standing wave, but also highlights the various modes of instability inherent to w_1 and w_2 . The behavior of methanol illustrates a strong tendency to instability in the form of a standing wave, while this feature is less pronounced in the dynamics of toluene. For example, panels (b), (d) and (f) show that the alternation of hot and cold spots in methanol is almost uniform in time. Entirely, in the

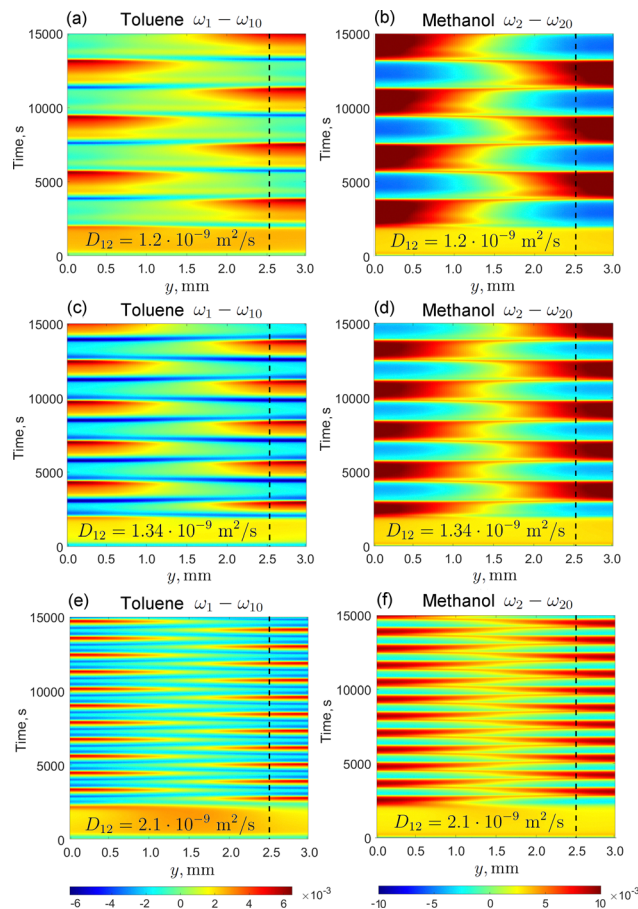


Fig. 12 Space-time maps presenting the amplitude of oscillation ($w_i - w_{i0}$) of toluene and methanol at $y = 2.5 \text{ mm}$ plane for different values of cross-diffusion: (a) and (b) $D_{12} = 1.2 \times 10^{-9} \text{ m}^2 \text{ s}^{-1}$, (c) and (d) $D_{12} = 1.34 \times 10^{-9} \text{ m}^2 \text{ s}^{-1}$ and (e) and (f) $D_{12} = 2.1 \times 10^{-9} \text{ m}^2 \text{ s}^{-1}$. The maps illustrate the presence of a standing wave for both components, but more pronounced for w_2 . The plots are built slightly outside the column center $x = 0.255 \text{ mm}$ and at $z = 24 \text{ mm}$. Black dashed lines correspond to the point, where the oscillations are shown in Fig. 11.

case of toluene, we observe an alternation of hot and cold regions, but the blue bands attributed to the secondary swinging instability, which are very thin, highlight the rapid changes. Even though the swinging occurs twice per period, at a small cross-diffusion, *i.e.*, $D_{12} = 1.2 \times 10^{-9} \text{ m}^2 \text{ s}^{-1}$ (panel a), only one of the bands is visible, since the amplitude of another one is small. At large D_{12} (see panel e), two blue bands are clearly visible, since the amplitude of both swings is similar. An undeniable positive sign of the space-time maps is that their comparison (from top to bottom) clearly shows that the oscillation frequency depends drastically on D_{12} .

Another benefit of such maps is that they provide information about the wavelength λ of perturbations. In the y direction λ is twice the net depth, *i.e.* $\lambda \sim 2L_y$, for all considered D_{12} , so it suggests that we are dealing with long-wavelength instability.

4.5 Mechanism of instability

The effect of cross-diffusion in the presence of thermodiffusion can modify the spatiotemporal patterns obtained under

different parametric conditions. Our study evidenced that oscillatory instability occurs only within a limited range of D_{12} values.

It is of interest to compare more carefully the waveform of oscillations at different D_{12} that are shown in the insets in Fig. 13 superimposed on the curve for the oscillation period. The depth of the peaks on the negative side (highlighted by the red arrows) quantifies the depletion of the heavier component (toluene) in the upper part of the column, *i.e.*, at point *P*. The general trend is that as D_{12} decreases, this peak shifts upwards, and as D_{12} increases, it drops. Note that the distance between the peaks roughly corresponds to the duration of the diffusion phase. Careful comparison of the first two insets clearly shows that the diffusion phase at a smaller D_{12} is much longer than at the reference point (the second inset). Another observation is that the change in $(w_1 - w_{1,0})$ during this phase tends to zero. The second component, highly enriched in the upper part during the diffusion phase, maintains the mass fraction almost constant, see Fig. 14. The elongated diffusion phase with passive behavior of both components leads to satiation when convection dominates diffusion and, starting from $D_{12} = 1.1 \times 10^{-9} \text{ m}^2 \text{ s}^{-1}$, the restoring force of w_1 cannot trigger new swings. The oscillations decay and the flow becomes stationary albeit with the density distribution in the form of stripes in *yz*-plane (see the patterns on the left in Fig. 14), which is maintained by the three-dimensional convective flow.

Fig. 14 summarizes, in terms of oscillation period and a compositional pattern, the different ways how a ternary mixture with the Soret effect responds to a change in D_{12} cross-diffusion coefficient. It is noteworthy that the swinging instability is triggered by the sign difference of the Soret and thermodiffusion in ternary mixtures. Hence, minor local changes around the mixture composition completely modify the global stability. As D_{12} decreases, the difference between the Soret and

thermodiffusion signs still persists, but the purely diffusive flux of the first component ($D_{11}\nabla C_1 + D_{12}\nabla C_2$) decreases. Regardless of the cross-diffusion, D_{11} is four times greater than D_{22} and thermodiffusion in the presence of convection can lead to the emergence of Turing-type instability with stationary patterns. A Turing instability occurs when the diffusion rates of two or more interacting species are different. The mechanism behind Turing instability is based on the interactions between two or more diffusing substances that react with each other in a nonlinear fashion. The transport of these species is also influenced by convection. It can lead to the formation of intricate spatial patterns such as stripes, spots, or spirals.

In the system under consideration, such a spatial pattern takes the form of stripes as shown on the left side of Fig. 14. Recently, Ghosh⁴⁴ reported about a notable effect of thermodiffusion on the pattern selection in the Turing instability. Among others, the patterns in the form of striped heterogeneity were observed. In our experiments, this type of pattern was observed in state point #3, where cross-diffusion is smaller, see Fig. 1. The agreement between the experiment and computer simulations is remarkable taking into account that the coefficients in the numerical model were taken from very different sources but not from the experiment under consideration.

Returning to Fig. 13 and moving towards larger D_{12} from the reference point, one can see from the insets that the diffusion phase is narrowing. In addition, the first peak goes down, and at the last inset, both peaks have the same value. This means that over the oscillation period, the levels of depletion and enrichment of toluene in the upper part of the TGC are somewhat similar. We can suggest that diffusion effects start to dominate convection. Shortly after that, the standing wave instability decays, the oscillations cease and the instability becomes monotonic. This direction corresponds to the growth of the positive net separation ratio Ψ . The stationary patterns

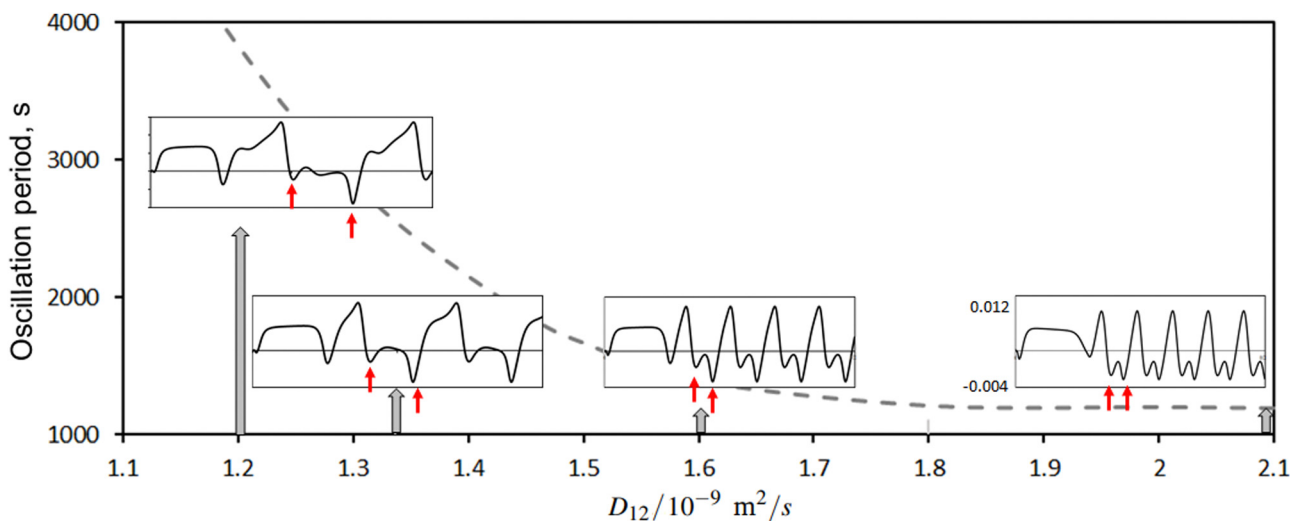


Fig. 13 The oscillation period (the dashed grey curve) and waveform evolution of toluene ($w_1 - w_{1,0}$) with D_{12} . Oscillations in all insets were recorded for 8000 s and have the same vertical scale, which is shown for clarity only in the last inset. Vertical grey arrows indicate the D_{12} values, to which the insets correspond. The two small red arrows on all the insets correspond to the swinging occurrence during the oscillation period: the first arrow approximately corresponds to the end of the first swinging, and the next to the beginning of the second one.

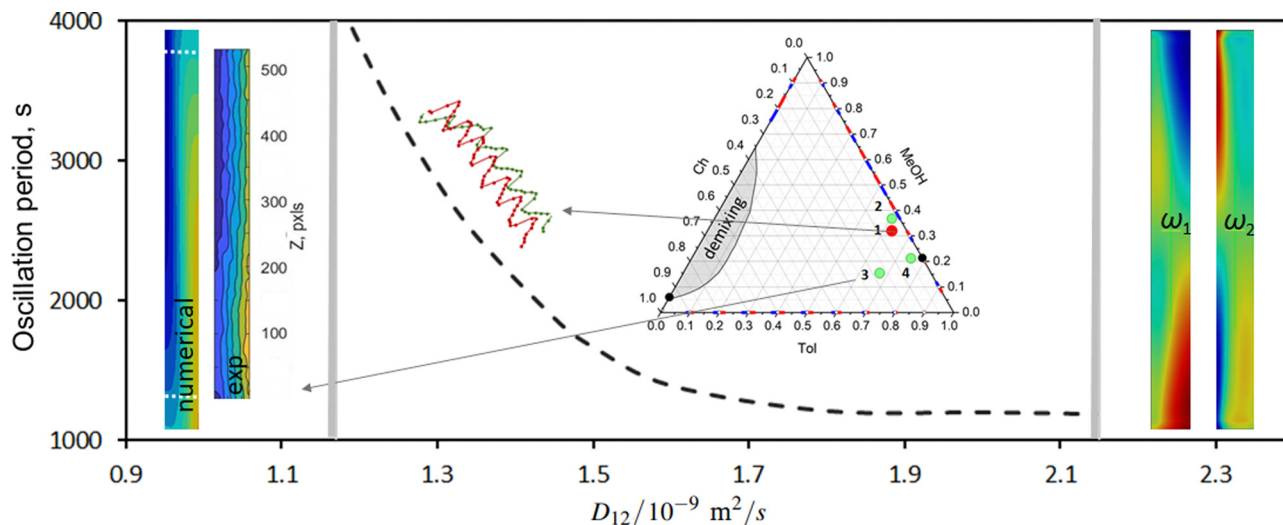


Fig. 14 Overview of the instabilities observed in a ternary mixture with the Soret effect placed in the TGC under the influence of cross-diffusion. This map shows consistency of the experimentally observed and the numerically obtained patterns with the change in D_{12} . The central part corresponds to the emergence of an oscillatory instability. The patterns on the left side correspond to $D_{12} = 1.1 \times 10^{-9} \text{ m}^2 \text{ s}^{-1}$ and, presumably, it is related to Turing-type instability. Both patterns are given in terms of optical phase distribution in the yz -plane. To do this, the numerical results were recalculated to the optical phase according to eqn (8) and (9). The experimental pattern is shorter because the optical window does not cover the full height of the TGC. The patterns on the right side are of numerical origin when $D_{12} = 2.3 \times 10^{-9} \text{ m}^2 \text{ s}^{-1}$ and indicate a monotonic instability.

for this case are shown on the right side of Fig. 14. The topology of these patterns presents a multi-cellular structure.

5 Conclusions

Cross-diffusion in ternary mixtures can modify the connection between the Soret and thermodiffusion effects, trigger secondary instability and can control the stability of the entire system. We have carried out an experimental and 3D numerical study of the response of toluene–methanol–cyclohexane ternary mixture with the Soret effect to a change in cross-diffusion coefficient D_{12} . The mixture is placed in a thermogravitational column, the two opposite walls of which are maintained at different temperatures. The interest in this study is driven by the ISS experiment at a selected point of the mixture, here called the reference point. The measurements revealed a curious finding that the first component, toluene, has a positive Soret coefficient S'_{T1} but its thermodiffusion coefficient D'_{T1} is negative due to large cross diffusion, D_{12} . The convective flow transports species segregated by the Soret effect in a direction according to the D_T sign, which can interact with the cross-diffusion effects. This creates complex coupling between the species leading to intricate spatial patterns and oscillations.

The laboratory experiments were carried out in the vicinity of the reference point. In this region, our experiments revealed different types of the system behavior – absence of the Soret effect, a stationary state that allows recovering the Soret coefficients, oscillatory instability, and Turing-type instability. For the first time, our experiments evidenced oscillatory instability in the Soret driven ternary system in TGC, which is favourably confirmed by the numerical simulations.

Numerical simulation provides insight into the mechanism of instability and indicates that a large cross-diffusion is responsible for the occurrence of a long-wave oscillatory instability in transverse direction. Furthermore, we have shown that the mismatch in signs between S'_{T1} and D'_{T1} due to large D_{12} is responsible for the secondary instability in the form of swinging motion of w_1 pattern, and, in addition, this is the motor of the entire oscillatory instability. Our study showed that oscillatory instability exists only within a limited range of the D_{12} values and then it decays to a different type of instability. It seems that the stationary pattern of Turing-type instability emerges at small D_{12} , while monotonic instability occurs at large D_{12} . These results may stimulate the study of Turing-type instability in ternary mixtures with the Soret effect and very different diffusion coefficients.

Conflicts of interest

There are no conflicts to declare.

Acknowledgements

The work is supported by KK-2023/00016 – M4SMART (Research Group Program) and PRE-2019-1-0202 of the Basque Government and PID2020-115086GB-C33 financed by MCIN/AEI of the Spanish Government.

Notes and references

- 1 A. Mialdun, M. Bou-Ali and V. Shevtsova, *Sci. Rep.*, 2021, **11**, 17735.

- 2 M. Schraml, H. Bataller, C. Bauer, M. M. Bou-Ali, F. Croccolo, E. Lapeira, A. Mialdun, P. Möckel, A. T. Ndjaka, V. Shevtsova and W. Köhler, *Eur. Phys. J. E: Soft Matter Biol. Phys.*, 2021, **441**, 128.
- 3 M. Gebhardt and W. Köhler, *J. Chem. Phys.*, 2015, **142**, 084506.
- 4 A. Mialdun, J.-C. Legros, V. Yasnou, V. Sechenyh and V. Shevtsova, *Eur. Phys. J. E: Soft Matter Biol. Phys.*, 2015, **38**, 27.
- 5 T. Lyubimova and N. Zubova, *Microgravity Sci. Technol.*, 2014, **26**, 241–247.
- 6 T. Lyubimova, N. Zubova and V. Shevtsova, *Eur. Phys. J. E: Soft Matter Biol. Phys.*, 2017, **40**, 27.
- 7 M. Braibanti, *et al.*, *Eur. Phys. J. E: Soft Matter Biol. Phys.*, 2019, **42**, 86.
- 8 M. M. Bou-Ali, A. Ahadi, D. A. D. Mezquia, Q. Galand, M. Gebhardt, O. Khlybov, W. Köhler, M. Larrañaga, J. C. Legros, T. Lyubimova, A. Mialdun, I. Ryzhkov, M. Z. Saghir, V. Shevtsova and S. V. Vaerenbergh, *Eur. Phys. J. E: Soft Matter Biol. Phys.*, 2015, **38**, 30.
- 9 Q. Galand, S. Van Vaerenbergh, W. Köhler, O. Khlybov, T. Lyubimova, A. Mialdun, I. Ryzhkov, V. Shevtsova and T. Triller, *J. Chem. Phys.*, 2019, **151**, 134502.
- 10 A. Mialdun and V. Shevtsova, *J. Chem. Phys.*, 2015, **143**, 224902.
- 11 A. Mialdun, I. Ryzhkov, O. Khlybov, T. Lyubimova and V. Shevtsova, *J. Chem. Phys.*, 2018, **148**, 044506.
- 12 T. Triller, H. Bataller, M. M. Bou-Ali, M. Braibanti, F. Croccolo, J. M. Ezquerro, Q. Galand, J. Gavalda, E. Lapeira, A. Laverón-Simavilla, T. Lyubimova, A. Mialdun, J. M. Ortiz de Zárate, J. Rodríguez, X. Ruiz and V. Shevtsova, *Microgravity Sci. Technol.*, 2018, **42**, 27.
- 13 T. Triller, D. Sommermann, M. Schraml, F. Sommer, E. Lapeira, M. M. Bou-Ali and W. Köhler, *Eur. Phys. J. E: Soft Matter Biol. Phys.*, 2019, **42**, 27.
- 14 A. Mialdun, H. Bataller, M. M. Bou-Ali, M. Braibanti, F. Croccolo, A. Errarte, J. M. Ezquerro, Y. Gaponenko, L. García-Fernández, J. J. Fernández, J. Rodríguez and V. Shevtsova, *Eur. Phys. J. E: Soft Matter Biol. Phys.*, 2019, **42**, 87.
- 15 A. Errarte, M. Schraml, W. Köhler, V. Shevtsova, M. M. Bou-Ali and A. Mialdun, *J. Chem. Eng. Data*, 2022, **67**(9), 2160–2173.
- 16 L. García-Fernández, H. Bataller, P. Fruton, C. Giraudet, A. Vailati and F. Croccolo, *Eur. Phys. J. E: Soft Matter Biol. Phys.*, 2022, **45**, 52.
- 17 A. Leahy-Dios, M. M. Bou-Ali, J. K. Platten and A. Firoozabadi, *J. Chem. Phys.*, 2005, **122**, 234502.
- 18 M. Larrañaga, M. M. Bou-Ali, I. Lizarraga, J. A. Madariaga and C. Santamaria, *J. Chem. Phys.*, 2015, **143**, 024202.
- 19 B. Šeta, E. Lapeira, J. Gavalda, M. M. Bou-Ali and X. Ruiz, *Microgravity Sci. Technol.*, 2021, **33**, 18.
- 20 A. Mialdun, J. Legros, V. Yasnou, V. Sechenyh and V. Shevtsova, *Eur. Phys. J. E: Soft Matter Biol. Phys.*, 2015, **38**, 27.
- 21 E. Lapeira, A. Mialdun, V. Yasnou, P. Aristimuño, V. Shevtsova and M. Bou-Ali, *Microgravity Sci. Technol.*, 2018, **30**, 635–641.
- 22 A. Zebib, *J. Chem. Phys.*, 2008, **129**, 134711.
- 23 I. I. Ryzhkov and V. M. Shevtsova, *Phys. Fluids*, 2009, **21**, 014102.
- 24 I. I. Ryzhkov and V. M. Shevtsova, *Phys. Rev. E: Stat., Non-linear, Soft Matter Phys.*, 2009, **79**, 026308.
- 25 T. Lyubimova, N. Lobov and V. Shevtsova, *Eur. Phys. J. E: Soft Matter Biol. Phys.*, 2018, **41**, 23.
- 26 I. I. Ryzhkov and V. M. Shevtsova, *Phys. Fluids*, 2007, **19**, 027101.
- 27 T. Grossmann and J. Winkelmann, *J. Chem. Eng. Data*, 2009, **54**, 405–410.
- 28 T. Grossmann and J. Winkelmann, *J. Chem. Eng. Data*, 2009, **54**, 485–490.
- 29 T. Janzen and J. Vrabec, *Ind. Eng. Chem. Res.*, 2018, **57**, 16508–16517.
- 30 S. Prokopev, T. Lyubimova, A. Mialdun and V. Shevtsova, *Phys. Chem. Chem. Phys.*, 2021, **23**, 8466–8477.
- 31 V. Shevtsova, C. Santos, V. Sechenyh, J.-C. Legros and A. Mialdun, *Microgravity Sci. Technol.*, 2014, **25**, 275–283.
- 32 B. Seta, A. Errarte, I. I. Ryzhkov, M. M. Bou-Ali and V. Shevtsova, *Phys. Fluids*, 2023, **35**, 021702.
- 33 S. Kozlova, A. Mialdun, I. Ryzhkov, T. Janzen, J. Vrabec and V. Shevtsova, *Phys. Chem. Chem. Phys.*, 2019, **21**, 2140–2152.
- 34 A. Mialdun and V. Shevtsova, *Int. J. Heat Mass Transfer*, 2008, **51**, 3164–3178.
- 35 A. Mialdun and V. Shevtsova, *J. Chem. Phys.*, 2011, **134**, 044524.
- 36 V. Shevtsova, V. Sechenyh, A. Nepomnyashchy and J. C. Legros, *Philos. Mag.*, 2011, **91**, 3498–3518.
- 37 M. Gebhardt and W. Köhler, *Eur. Phys. J. E: Soft Matter Biol. Phys.*, 2015, **38**, 24.
- 38 P. Naumann, A. Martin, H. Kriegs, M. Larrañaga, M. M. Bou-Ali and S. Wiegand, *J. Phys. Chem. B*, 2012, **116**, 13889–13897.
- 39 B. Seta, PhD thesis, Universitat Rovira i Virgili, Tarragona, Spain, 2020.
- 40 J. K. Platten and J. C. Legros, *Convection in liquids*, Springer-Verlag, Berlin, 1984.
- 41 K. B. Haugen and A. Firoozabadi, *J. Chem. Phys.*, 2005, **122**, 014516.
- 42 G. Guevara-Carrion, Y. Gaponenko, T. Janzen, J. Vrabec and V. Shevtsova, *J. Phys. Chem. B*, 2016, **120**, 12193–12210.
- 43 G. Guevara-Carrion, Y. Gaponenko, A. Mialdun, T. Janzen, V. Shevtsova and J. Vrabec, *J. Chem. Phys.*, 2018, **149**, 064504.
- 44 P. Ghosh, *Phys. Rev. E*, 2019, **100**, 042217.